The Astrophysical Journal, 994:121 (16pp), 2025 November 20 https://doi.org/10.3847/1538-4357/adfbe1
© 2025. The Author(s). Published by the American Astronomical Society.
OPEN ACCESS

The Serpent Eating Its Own Tail: Dust Destruction in the Apep Colliding Wind Nebula

Ryan M. T. White[1,2], Benjamin J. S. Pope[1,2], Peter G. Tuthill[3], Yinuo Han[4], Shashank Dholakia[2], Ryan M. Lau[5,6], Joseph R. Callingham[7,8], and Noel D. Richardson[9]
[1] School of Mathematical and Physical Sciences, Macquarie University, Sydney, 2113 NSW, Australia; ryan.white@mq.edu.au
[2] School of Mathematics and Physics, University of Queensland, Brisbane, 4072 QLD, Australia
[3] Sydney Institute for Astronomy, School of Physics, University of Sydney, Sydney, 2006 NSW, Australia
[4] Division of Geological and Planetary Sciences, California Institute of Technology, 1200 East California Boulevard, Pasadena, CA 91125, USA
[5] NSF NOIRLab, 950 North Cherry Avenue, Tucson, AZ 85719, USA
[6] IPAC, Mail Code 100-22, Caltech, 1200 East California Boulevard, Pasadena, CA 91125, USA
[7] ASTRON, Netherlands Institute for Radio Astronomy, Oude Hoogeveensedijk 4, Dwingeloo, 7991 PD, The Netherlands
[8] Anton Pannekoek Institute for Astronomy, University of Amsterdam, Science Park 904, 1098 XH Amsterdam, The Netherlands
[9] Department of Physics and Astronomy, Embry-Riddle Aeronautical University, 3700 Willow Creek Road, Prescott, AZ 86301, USA
Received 2025 June 11; revised 2025 August 7; accepted 2025 August 8; published 2025 November 19

Abstract

Much of the carbonaceous dust observed in the early Universe may originate from colliding wind binaries (CWBs) hosting hot, luminous Wolf–Rayet (W-R) stars. Downstream of the shock between the stellar winds there exists a suitable environment for dust grain formation, and the orbital motions of the stars wrap this dust into richly structured spiral geometries. The Apep system is the most extreme W-R CWB in our Milky Way: two W-R stars produce a complex spiral dust nebula, whose slow expansion has been linked to a gamma-ray burst progenitor. It has been unclear whether the O-type supergiant 0.″7 distant from the W-R + W-R binary is physically associated with the system, and whether it affects the dusty nebula. Multiepoch Very Large Telescope/VISIR and JWST/MIRI observations show that this northern companion star routinely carves a cavity in the dust nebula—the first time such an effect has been observed in a CWB—which unambiguously associates the O star as a bound component to the Apep system. These observations are used together with a new geometric model to infer the cavity geometry and the orbit of the W-R + W-R binary, yielding the first strong constraints on wind and orbital parameters. We confirm an orbital period of over 190 yr for the inner binary—nearly an order of magnitude longer than the next longest-period dust-producing W-R CWB. This, together with the confirmed classification as a hierarchical triple, cements Apep as a singular astrophysical laboratory for studying colliding winds and the terminal life stages of the most massive star systems.

Unified Astronomy Thesaurus concepts: Massive stars (732); Wolf-Rayet stars (1806); Circumstellar dust (236); Stellar winds (1636); Dust nebulae (413)

1. Introduction

Colliding wind binaries (CWBs) are some of the most extreme astrophysical environments known, where hot shocks are formed from the collision of massive stellar winds. A rare subclass of these systems harbor a Wolf–Rayet (W-R) star together with a massive, main-sequence OB companion. A handful of such binaries in the Galaxy are known to host WC-subtype W-Rs and are often the site of copious dust production (R. M. Lau et al. 2020; R. M. T. White & P. Tuthill 2025). This dust is produced from the shock of the colliding winds from the two stars, which offers an environment that nurtures dust nucleation through mixing of wind material at the contact discontinuity and self-shielding from the radiation of the massive stars (V. V. Usov 1991; A. Soulain et al. 2023), although the exact mechanisms by which dust formation is mediated by the colliding winds remains an open question. The orbital motion of the two stars then wraps the outflowing dust plume into intricate spiral nebulae, which encode the dynamical history of the stars, as well as their wind physics (P. G. Tuthill et al. 1999, 2008). Although rare in the present-day Galaxy, these binaries are thought to have been a dominant contributor of carbonaceous dust in the Milky Way's early history and they offer a convincing explanation for structured circumstellar material seen in extragalactic supernova light curves (T. Moore et al. 2023).

Of all the CWBs in the Galaxy, the Apep system stands out as the most puzzling; it is, at present, the only spectroscopically confirmed classical W-R + W-R system to host a WC-type star, while its orbital period is the longest (by an order of magnitude) among the dusty CWBs (J. R. Callingham et al. 2019, 2020). In addition to, or perhaps because of this, the Apep system is a test bed of CWB physics across the electromagnetic spectrum; besides the infrared plume, the colliding winds result in unusually luminous nonthermal emission from high energies (in the X-ray; S. del Palacio et al. 2023; S. A. Zhekov & B. V. Petrov 2025) to radio wavelengths (J. R. Callingham et al. 2019; S. Bloot et al. 2022; L. N. Driessen et al. 2024), with the nonthermal colliding wind shock itself having been imaged with very long baseline interferometry (B. Marcote et al. 2021) cementing it as the most luminous nonthermal CWB. These multiwavelength studies have propelled Apep into being one of the most well-studied CWBs even within the first 10 yr of its discovery.

One of the most intriguing open questions about the Apep nebula is the apparent discrepancy between the proper-motion expansion rate and the spectroscopic wind speeds of its component stars. Spectroscopy clocks the two winds at speeds

Original content from this work may be used under the terms of the Creative Commons Attribution 4.0 licence. Any further distribution of this work must maintain attribution to the author(s) and the title of the work, journal citation and DOI.

of $2100 \pm 200\,\mathrm{km\,s^{-1}}$ and $3500 \pm 100\,\mathrm{km\,s^{-1}}$ (independent of a distance estimate), while the nebula expansion speed as measured by the proper motion of the dust is much slower at $910 \pm 120\,\mathrm{km\,s^{-1}}$ assuming a distance of 2.4 kpc (J. R. Callingham et al. 2020; Y. Han et al. 2020). Potential resolutions for these apparently contradictory values have been proposed, including an incorrect distance measurement, anisotropic winds in one or both of the central W-R stars, complex wind braking physics at the shock front, or some combination of these.

There is also some uncertainty as to whether the "northern companion" to Apep, an O Iaf supergiant 0.″7 distant from the central W-R + W-R binary, is dynamically associated with the system. It is highly unlikely for a field star of this rare type to so closely coincide along the line of sight, and there is a similar dust extinction of this star compared to the central binary, which suggests the same distance (J. R. Callingham et al. 2020). Despite this, there has not yet been a definitive association of the star to the Apep system in large part due to the failure of previous studies to point to evidence of impacts on the dusty nebula as would be expected to be generated by a massive luminous star in close proximity.

Geometric modeling has so far been the workhorse tool in understanding the binary orbit of the "Pinwheel" CWBs (P. G. Tuthill et al. 2008; R. M. T. White & P. Tuthill 2025), and indeed Apep's orbit. The goal of such modeling is to understand the geometric structure of the dust nebula and the orbits of the stars at its center, while hydrodynamic modeling of CWBs is a more useful tool to understand the processes leading to dust formation (e.g., as in J. W. Eatson et al. 2022a; A. Soulain et al. 2023). The dust produced along the surface of the wind–wind shock is wrapped into a spiral from the orbital motion of the stars, which can be modeled with a geometric prescription based on the orbital elements.

Until now, only the single innermost dust shell of Apep has been observed (with the Very Large Telescope (VLT)/VISIR instrument), leading to ambiguity between orbital and nebula expansion parameters, some of which being highly covariant in model fits. Observations of older, concentric outer shells are capable of resolving this degeneracy. A dramatic illustration of this came recently from James Webb Space Telescope (JWST) Mid-infrared Instrument (MIRI) images that revealed over a dozen concentric shells of material around the WR 140 system (R. M. Lau et al. 2022; E. P. Lieb et al. 2025). Given that each shell corresponds to one periastron passage of the central stars, this image represents ∼170 yr of dynamical history and yields an unambiguous orbital solution that agrees with the 3D orbit of the system of J. D. Thomas et al. (2021) and R. M. Lau et al. (2022). In the time since, four more W-R CWBs have been observed with JWST: WR 48a, WR 112, WR 125, and WR 137 (N. D. Richardson et al. 2025), which have revealed the faint thermal emission of centuries old dust.

In this paper we present a strongly constrained orbital solution to the central W-R + W-R binary of the Apep system using the three nested concentric dust shells revealed by JWST/MIRI imaging (Y. Han et al. 2025). We also employ these new data, together with multiple earlier epochs of VISIR imaging, to definitively link the O supergiant as a dynamically bound third member of the Apep hierarchical triple system through the cavity it carves in the wider nebula. These findings were generated by way of a state-of-the-art geometric code, described in Appendix B, capable of modeling the impact of higher-order effects such as dust acceleration and wind anisotropy.

2. Methods

2.1. Apep Direct Images

The Apep system was observed with JWST/MIRI as part of the JWST GO Program 5842 on 2024 July 24 for 3.64 hr, using the F770W, F1500W, and F2550W filters. We show a false-color composite image using these filters in Figure 1 following the reduction process of Y. Han et al. (2025) and Appendix A.1.

In addition to the multiwavelength JWST images taken, Apep was imaged with the VLT/VISIR instrument in 2024 June, bringing the total number of VISIR Apep epochs to four spanning the years 2016 to 2024. All VISIR images used in this study were taken in the J8.9 band, which is centered at 8.7 μm. The data reduction for the VLT images is described in more detail in Y. Han et al. (2025).

2.2. Geometric Model

We have developed a new and fast colliding wind nebula geometric model, `xenomorph` (R. M. T. White 2025)—which is motivated by the new VLT and JWST imagery of Apep—that can be applied to any CWB with resolved dust spirals. The basic principle is similar to previous geometric codes, e.g., that in Y. Han et al. (2022), although our new code is ∼100 times more performant due to our using the JAX framework for Python (J. Bradbury et al. 2018), as well as featuring more physical parameters, being more user friendly, and better documented. The open-source code is available at github.com/ryanwhite1/xenomorph. We describe the physical features of the code and their motivation in Appendix B, and in this section we describe how we have used the software in the context of our Apep imagery.

2.2.1. Parameter Estimation with the Geometric Model

Geometric models are a key tool in learning about the orbital parameters of the binary stars at the heart of colliding wind nebulae. Fitting for these orbital and wind parameters involves forward modeling the nebula, changing parameters until the ridge geometry best aligns with that which is observed; because of this, we need not consider the precise dust properties (as described in a companion paper; Y. Han et al. 2025), only its density structure. That is, the simulated images reproduce the projected (and normalized) column density of dust in the nebula, and not its luminosity, temperature, or other quantities which require deeper modeling.

The `xenomorph` code was designed with Bayesian parameter inference in mind, such as Markov Chain Monte Carlo (MCMC) or Hamiltonian Monte Carlo (HMC). However, there are too many parameters to fit for when using a conventional MCMC algorithm (which struggles or fails with high dimensionality; D. Huijser et al. 2015), which leaves gradient-based methods like HMC as the only option. Although the code computes gradients in the model via autodifferentiation with JAX, the gradients are unstable and are not suitable for such a method. In addition to this, it is difficult to describe an informative goodness-of-fit function for the fitting, given that the geometric model does not account for the radiative transfer and thermal emission of the nebula (where doing so would make the computational cost

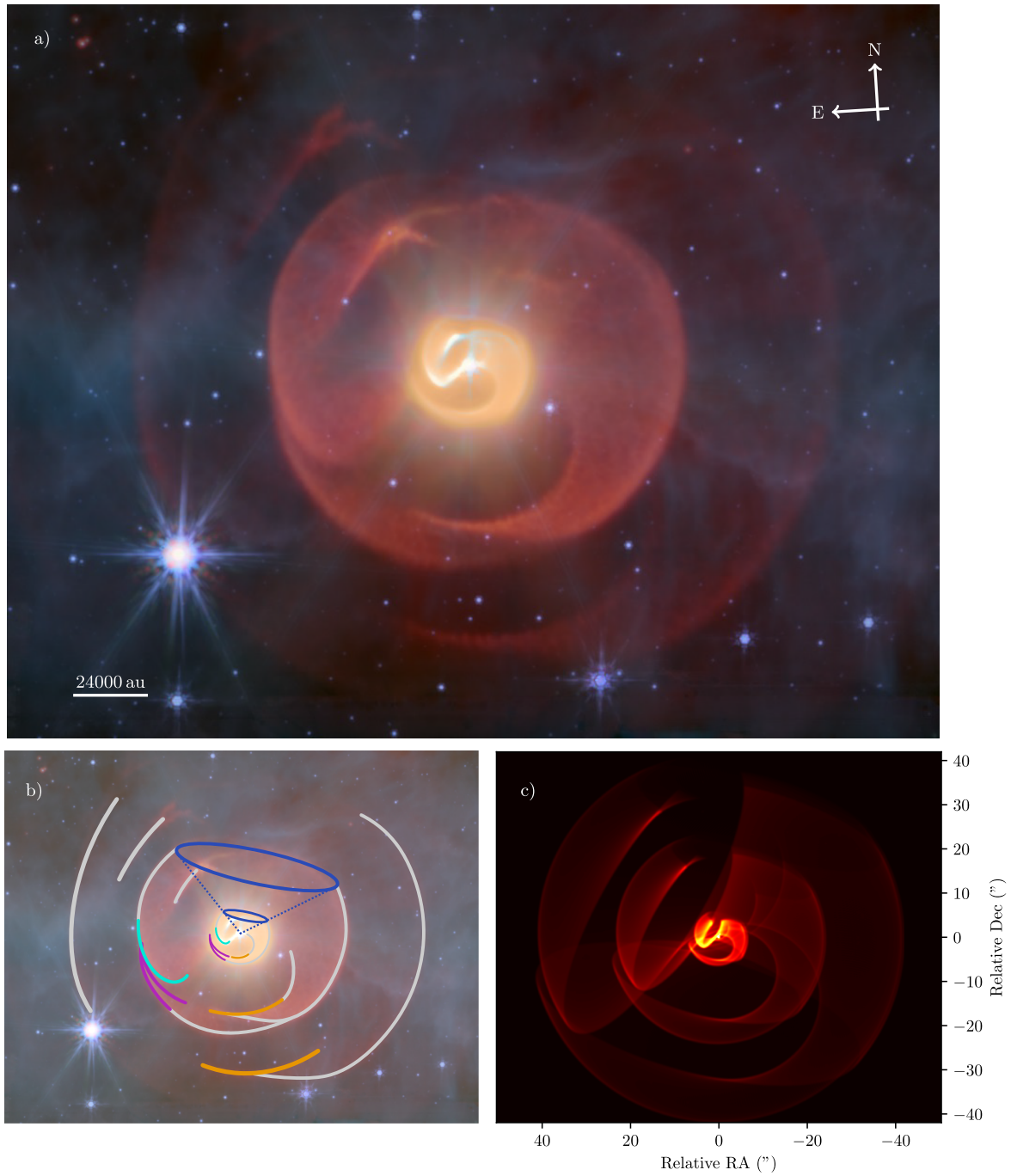

Figure 1. Panel (a) shows the false-color composite image of the Apep nebula made by combining data from the F770W, F1500W, and F2550W filters. Three concentric shells of dust are clearly seen, with faint evidence of a fourth at the edge of frame. The W-R + W-R central engine and the tertiary O supergiant lie in the center of frame, while the bright star in the lower left is not associated with the Apep system. The processing procedure is described in Appendix A.1. In panel (b) we highlight the concentric shell structure with a gray skeleton, where the colored ridges indicate regions of interest: the position of the cavity across concentric shells (see Figure 3), the relative positions of the southeast ridge coinciding with the southeast tail over time are key for the new eccentricity value, and the southern bar aids in the period determination. Panel (c) shows our geometric fit to the three visible shells of Apep, where the alignment of the modeled to the observed shells is shown in Figure 2.

intractable for fitting). With this in mind, we manually fit for the parameters using the difference imaging within the graphical user interface built into the `xenomorph` model, to best align the nebula structure. We describe below the parameter-specific choices we made in this fitting process.

Orbital and system parameters. We begin fitting for the imprint of the W-R + W-R binary orbit on the nebula using the previous best values in the literature (most notably those in Y. Han et al. 2020). We treat the orbital eccentricity, inclination, longitude of ascending node, argument of periastron, and orbital phase as free parameters. We adopt the orbital period of Y. Han et al. (2025), which was found via a proper-motion analysis of dust ridge expansion. The orbital semimajor axis and stellar masses are unconstrained by geometric modeling of the nebula at this spatial scale and so cannot be fit for. We adopt a distance of 2.4 kpc (J. R. Callingham et al. 2019; Y. Han et al. 2020) to the system, which sets the nebula expansion speed as a fixed parameter when coupled with the adopted orbital period (due to

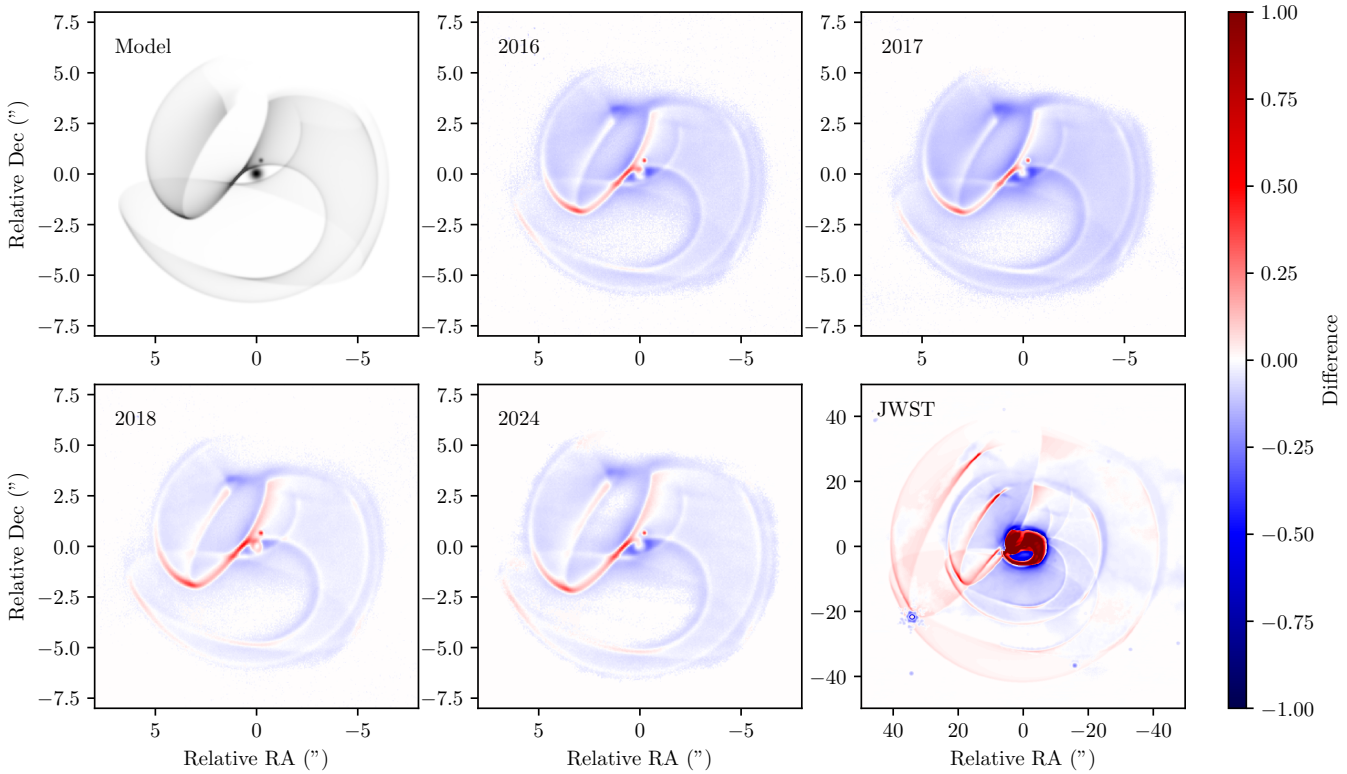

Figure 2. Using the four VLT epochs plus the 25.5 μm JWST image, we found parameters for our geometric model that faithfully reproduce the observed geometry; the numerical values of each parameter are shown in Table 1. The top left panel shows the model geometry at ϕ_{2024}, and all other panels show the difference imaging of $F_{\rm model} - F_{\rm obs}$ adjusted for the respective orbital phases; note that the JWST panel (bottom right) is over a larger angular scale. Although the exact flux often does not entirely cancel out in the difference imaging, we note the nebula ridge positions—which encode all of the fit parameters—align very well. We have an animation available online that shows the evolution of a shell with our parameters over one orbital period.

the trigonometry of the nebula expanding in the plane of the sky).

Wind and dust parameters. We treat the shock cone open angle (describing the momentum ratio of the two W-R stellar winds), true anomaly of dust turn-on/off, and azimuthal dust variation as free parameters in fitting. We fixed the amplitude of azimuthal variation to $A_{\rm az} = 0.5$, which appeared to best match the data. The orbital modulation and gradual turn-on/off in dust production was not included in the fit in this study after initial tests with it did not appear to match the observations.

Tertiary cavity. As described in Section 3, we have found strong evidence of a cavity in the northeastern region of the Apep nebula. In constraining the geometry of this cavity (and hence the parameters of the tertiary star), we allowed the cavity open angle and the polar and azimuthal positions of the cavity to be free. The destruction constant was fixed to $A_{\rm tert} = 1.75$ although more negative values can just as suitably fit the observations. In modeling the position of the stellar sprites, we also allowed the distance of the tertiary star from the inner binary to be a free parameter. Our proposed phenomenology for the cavity is that it is a result of sculpting from the tertiary companion in Apep, however in fitting for the position of the cavity we only considered the nebular geometry itself and not the position of the tertiary star in the imagery.

Miscellaneous parameters. The nucleation distance of the dust with respect to the shock front is only constrained by high angular resolution observations of the inner core of CWBs. Given that our observations are over very large spatial scales, there is no way to constrain the nucleation distance from such direct images; regardless, the nucleation distance is only relevant in the geometric model at small spatial scales (on the order of the semimajor axis) as it dictates the distance at which dust first appears. Hence, we have fixed the nucleation distance to 0 au and note that this has no effect on the results for an episodic dust producer and at an orbital phase far from periastron passage. Additionally, the brightness and width of the Gaussian profiles of the stars in the image were treated as free parameters, and were scaled until they appeared to roughly match the relative brightnesses in the imagery. Finally, all simulated images (including the difference fits of Figure 2) in this study are convolved with a Gaussian blur with a width of 2 pixels to emulate the observation point-spread functions and the true "fluffiness" of the nebula edges.

3. Results

In this paper we are primarily concerned with modeling the geometric structure of the Apep nebula and how this constrains the binary orbit and stellar parameters. Figure 1 reveals three concentric shells of dust that closely match expanded versions of a single common structure, although with evidence for some degree of geometric evolution between them. The innermost shell cannot be mapped by a pure inflation to perfectly match the the older (outer) shells since the projected geometry evolves slightly over time as the 3D structure expands (see the linked animation in the Figure 2 caption). Each shell is the result of dust production coinciding with a periastron passage, so this image contains nearly a millennium of dynamical information about the Apep system.

Table 1
Our Best-fitting Parameters for the Apep System

Parameter	Value	References
Eccentricity, e	0.82 ± 0.04	W25
Inclination, i	$24° \pm 3°$	W25
Longitude of ascending node, Ω	$164° \pm 15°$	W25
Argument of periastron, ω	$10° \pm 10°$	W25
Opening angle, $\theta_{\rm OA}$	$126° \pm 5°$	H20, W25
Orbital period, $P_{\rm orb}$	193 ± 11 yr	H25, W25
Orbital phase at 2024 July, ϕ_{2024}	0.35 ± 0.02	W25
Distance, d	$2.4^{+0.2}_{-0.5}$ kpc	C19, H20
Dust shell expansion speed, $v_{\rm dust}$	1020 ± 100 km s^{-1}	H25, W25
Dust turn-on true anomoly, $\nu_{t_{\rm on}}$	$-108° \pm 10°$	W25
Dust turn-off true anomoly, $\nu_{t_{\rm off}}$	$141° \pm 10°$	W25
Azimuthal Variation, $\sigma_{\rm az}$	$30° \pm 10°$	W25

Note. The opening angle parameter $\theta_{\rm OA}$ is slightly updated from the reference, and we make no attempt to fit for the distance to the system. The dust expansion speed, $v_{\rm dust}$, is consistent with the 90 mas yr^{-1} found by the proper-motion analysis in Y. Han et al. (2025) when at a distance of 2.4 kpc. References: C19—J. R. Callingham et al. (2019); H20—Y. Han et al. (2020); H25—Y. Han et al. (2025); and W25—This work.

To analyze the structure of the Apep nebula, we developed a new computationally efficient geometric model that reproduces the dust morphology given orbital and stellar parameters (see Section 2.2). By fitting simulated structures to the images, we determined the system parameters shown in Table 1 with the fits to the images shown in Figure 2. The fitting was aided by multiple epochs of Apep imagery spanning 8 yr from the VLT, and the VLT images together with the JWST image allowed us to break any degeneracies between orbital phase, orbital period, and nebular expansion speed. When fitting with only a single epoch and a single shell, the ridge geometry can be suitably fitted by a range of degenerate orbital periods, expansion speeds and phases; more epochs of imaging and more visible shells thus greatly constrains the parameter space. The most surprising result of the fitting (and the proper-motion analysis in Y. Han et al. 2025), given by the separation between successive shells now revealed by JWST, is that the central W-R + W-R binary in the center of the Apep system must have an orbital period of 193 ± 11 yr—almost twice as long as previously thought based on analysis of the single innermost shell. We note that this period estimate is agnostic of distance—as it only relies on the shell spacing and angular expansion speed—although the geometric fitting of the period is covariant with expansion speed; simultaneously fitting the VISIR epochs plus the MIRI image places a lower bound of 170 yr for the orbital period, where periods below this cannot match the observed geometry evolution. This makes Apep by far the longest-period CWB to produce a dusty nebula at almost an order of magnitude longer than WR 48a (whose period is $\sim$32 yr; P. M. Williams et al. 2012). The shell spacing requires that the current orbital phase of the inner W-R + W-R binary be $\phi_{2024} = 0.35 \pm 0.02$ at the time of the JWST observation; this means that the last periastron passage would have occurred in the year 1956 ± 6 and the next in 2149 ± 9. Interestingly, the date of previous periastron passage is consistent with the previous estimate using the period of 125 yr and phase of $\sim$0.6 given in Y. Han et al. (2020). The conditions that allow copious dust production—and indeed its extended survival—in such a widely separated long-period system are not well understood, but the unique configuration of a double W-R star at the heart of Apep is likely a pivotal factor.

With successive outer dust shells now visible thanks to the sensitivity of JWST/MIRI, we are able to better understand how the dust geometry changes over time. Comparing the innermost (first) shell to the second shell, we can see that the relative spacing between the southeast ridge and southeast tail is reduced over time (Figure 1, panel (b)). This, together with the significantly earlier orbital phase estimate at 2024 ϕ_{2024}, means that the W-R + W-R binary must be on a more eccentric orbit to have reduced that separation by such a degree over 193 yr. We have found that $e = 0.82 \pm 0.04$ most accurately reproduces this ridge positioning across concentric shells. This propels Apep into a class of high-eccentricity CWBs such as WR 140 or WR 19 (P. M. Williams et al. 2009a, 2009b), where the conditions at the shock should change significantly over the course of the orbit. Still, the physical processes at the colliding wind shock in Apep are different from that of other W-R CWBs; Apep's shock should be adiabatically cooled throughout its whole orbit while systems such as WR 140 are radiatively cooled, particularly at periastron (E. R. Parkin & J. M. Pittard 2008). This has implications as to the conditions of dust production throughout Apep's orbit. With our parameters we find that dust production "turns on" at $\phi \simeq 0.97$ and "turns off" at $\phi \simeq 0.10$, which translates into a production period of $\sim$25 yr. We do not find any evidence of orbital modulation in dust production—as seen in WR 140 (Y. Han et al. 2022)—but some azimuthal variation in dust production (i.e., the trailing edge of the shock with respect to orbital motion favors dust production) makes for a closer geometric fit to the observed shells, consistent with WR 140 (Y. Han et al. 2022; R. M. Lau et al. 2022).

3.1. Physics of the Dust Cavity

One of the key open questions since the discovery of Apep is whether or not the "northern companion" star, an O8 Iaf supergiant 0.″7 north of the central W-R + W-R binary, is associated with the W-R stars and Apep nebula, or is a (statistically unlikely) apparent line-of-sight alignment. In analyzing archival VLT data, together with the new VLT epochs and JWST imagery, we have conclusively linked the O star to the W-R stars, identifying the Apep system as a hierarchical triple. The new evidence for this lies in an apparent "cavity" of dust along the direction of the tertiary star from the W-R + W-R binary. Figure 3 shows that by incorporating a "dust destruction" region along the surface of a cone into our geometric model, we may accurately explain the missing dust. The parameters of the destruction cone, in spherical coordinates relative to the orbital plane of the W-R + W-R binary, are shown in Table 2. We also note that adding a stellar sprite 1700 au from the inner binary at the 3D angular position of the cavity precisely matches the observed location of the tertiary star in Apep, further supporting the O star as the cavity sculptor. Due to the asymmetric nature of the Apep nebula, the angular position of the O star is uniquely associated with the position of the cavity and so there are no alternative configurations that can explain such cavity ridge positions.

Our proposed mechanism for this cavity is as follows. As the dust forms from the central W-R + W-R colliding wind shock, that material expanding radially northwards enters the environment of the O star companion. A large fraction of this

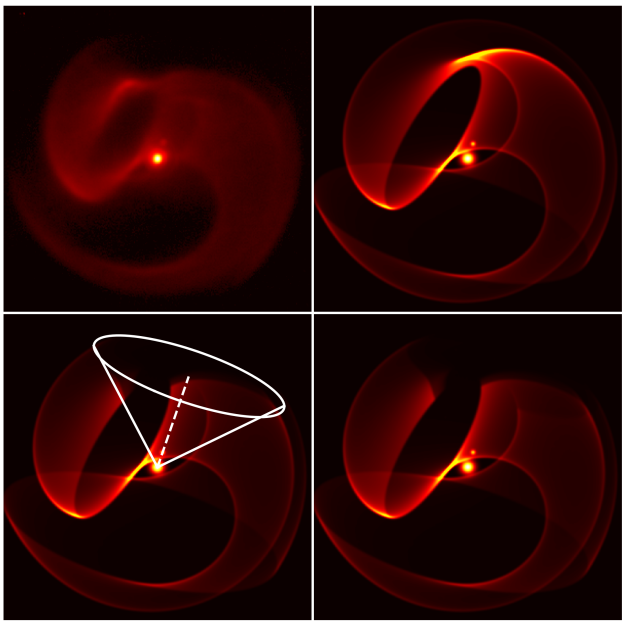

Figure 3. An illustration of the cavity carved by the northern O star companion in the Apep system. The W-R + W-R binary is the central bright point, while the northern companion is the smaller point source 0.″7 to the north. Top left: the innermost shell of the Apep nebula observed with VLT/VISIR, processed as in Appendix A.2. Top right: previous models with no dust destruction effects from the northern companion overestimate the dust luminosity in the upper region of the plume. Bottom left: we model dust destruction along the volume of a cone extending out of the W-R + W-R central engine along the line-of-sight vector to the northern companion. Bottom right: with the addition of this region of dust destruction, the model geometry now more closely matches what we see with direct imaging (top left).

Table 2
Parameters Describing the Simple Conical Model for the Dust Depletion Region of Apep due to the Northern Companion in an Ordinate System Relative to the Wolf–Rayet + Wolf–Rayet Binary Orbital Plane

Parameter	Value
Inclination angle, $\beta_{\rm tert}$	$124^\circ \pm 10^\circ$
Azimuthal angle, $\alpha_{\rm tert}$	$239^\circ \pm 10^\circ$
Opening angle, $\theta_{\rm OA,tert}$	$90^\circ \pm 10^\circ$
Tertiary star radial position, $r_{\rm tert}$	1700 ± 200 au

Note. An inclination angle of 0° lies directly below the orbital plane, while the periastron position of the inner binary is at 180° azimuthal angle. For the $r_{\rm tert}$ parameter, we assume the distance to Apep is $d = 2.4$ kpc.

northbound dust is destroyed and no longer contributes, carving a gap in the shell geometry. The dust then continues outward where the cavity persists as a scar indicative of earlier interaction with the tertiary star. Rather than destroyed, we investigated several scenarios where the dust is displaced but none could reconcile the observed geometry in the nebula (this is discussed further in Section 4.1).

The root cause of the apparent cavity of dust in the Apep nebula is almost certainly a combination of several processes in parallel. From our derived geometry of the cavity, we are able to discern some relative dominance between competing effects. The main pieces of information we have pertaining to the dust physics is that the cavity open angle is approximately $90^\circ \pm 10^\circ$, and that the O supergiant companion lies 1700 ± 200 au from the W-R + W-R central engine—with these two pieces of information together, we find that the radius of the cavity when the dust shell directly passes the O companion is also about 1700 au.

The first avenue to dust destruction we consider is grain sublimation as a result of radiative heating from the O star. For a UV source of brightness $L_{\rm UV}$ and grain sublimation temperature of $T_{\rm sub}$, T. Hoang et al. (2019) give the sublimation distance as

$$r_{\rm sub} \simeq 0.015 \left(\frac{L_{\rm UV}}{10^9 L_\odot}\right)^{1/2} \left(\frac{T_{\rm sub}}{1800\ {\rm K}}\right)^{-2.8} {\rm pc}. \quad (1)$$

For carbonaceous dust with sublimation temperature ~ 1800 K (R. M. Lau et al. 2023), and a source of UV luminosity $\sim 10^5$ $L_\odot$, we arrive at a sublimation radius of $\sim$30 au. This is 2 orders of magnitude smaller than the required dust destruction radius of $\lesssim$1700 au, and so grain sublimation cannot be the dominant process of dust destruction in the Apep nebula.

The second process of destruction we consider is by grain–grain or grain–ion collisions inducing grain shattering. O supergiant stars, like W-Rs, are characterized by fast and dense winds, so we would expect a significant wind–wind shock where the nebula intercepts the supergiant wind. To test whether we observe such a shock as expected, we consider the wind momentum ratio

$$\eta = \frac{\dot{M}_1 v_{\infty,1}}{\dot{M}_2 v_{\infty,2}}, \quad (2)$$

where $\dot{M}$ and v_∞ are the mass-loss rate and terminal wind speed of each star. This momentum ratio relates to the shock opening angle as

$$\eta_{\rm S/W} = \left(\frac{121}{\theta_{\rm OA}/2} - \frac{31}{90}\right)^3, \quad (3)$$

as given by P. G. Tuthill et al. (2008) and K. G. Gayley (2009), where $\eta_{\rm S/W}$ is the ratio of the stronger to the weaker wind, and $\theta_{\rm OA}$ is the shock opening angle. Inserting an opening angle of 90° yields a momentum ratio of $\eta_{\rm S/W} \sim 13$ for the mixed W-R + W-R wind to the O8 Iaf wind. If a wind–wind shock is the dominant influence on this cavity, we would expect to recover a similar wind momentum ratio with Equation (2). For this, we can use our nebular expansion speed of 1020 km s^{-1} and estimate a mass flux of $\sim 10^{-4}$–$10^{-4.75}$ $M_\odot$ yr^{-1}; the exact mass flux is difficult to discern since it is the mixed product of two W-R winds, each with different intrinsic mass-loss rates, but each should be independently in this range (J. R. Callingham et al. 2020). J. R. Callingham et al. (2020) give the terminal wind speed of the O star as 1280 ± 50 km s^{-1}, and if we assume a mass-loss rate in the range $10^{-5.2}$–10^{-6} $M_\odot$ yr^{-1} (typical for O supergiants of this spectral type; P. A. Crowther & C. J. Evans 2009), we can recover a wind momentum ratio of $\eta_{\rm S/W} \sim 13$ using Equation (2). This result implies that the cavity geometry may be explained at least partially by the presence of a tertiary shock with grain–ion sputtering. Although the radius of the cavity is 1700 au, the tertiary shock front will be significantly closer to the O star at the point of stagnation between the mixed W-R + W-R wind and the O star wind. Following B. Marcote et al. (2021) and J. Cantó

et al. (1996), the stagnation point will be at a distance

$$R_{\mathrm{W/S}} = \frac{r_{\mathrm{tert}}}{1 + \eta_{\mathrm{S/W}}^{1/2}}, \quad (4)$$

from the O star (with the weaker wind). Inputting our distance and wind momentum ratio values gives a distance of ∼370 au, which is still an order of magnitude too large for the dust destruction mechanism to be from dust sublimation. In Section 4.1 we describe more mechanisms that may be working in parallel on the dust grains within the cavity geometry.

4. Discussion and Conclusions

In light of the finding of accelerating dust shells of WR 140 (Y. Han et al. 2022), we incorporated dust acceleration for the first time into a geometric model. We chose a phenomenological prescription that can account for a range of smooth acceleration profiles as described in Appendix B.3. We find that there is no evidence of dust acceleration or deceleration in the dusty shells of the Apep nebula. The former result is expected, since this acceleration is expected to be significant due to radiation pressure only at very small orbital phases (which are not probed in our imagery; Y. Han et al. 2022), while the latter result indicates there are negligible drag forces acting on the shells as they expand into the interstellar medium (ISM). This in turn implies that the strong winds from this W-R system kinematically dominate the surrounding region at least to the limits of the shells we see. Our imagery also indicates that the dust from the Apep nebula is capable of surviving for at least $3P_{\mathrm{orb}} \simeq 600$ yr while subjected to the harsh ISM environment.

Since the discovery paper of the Apep nebula, there has been a puzzling contradiction between the measured nebular expansion and the spectroscopic wind speeds of the central W-R stars (J. R. Callingham et al. 2019). Our fitted expansion speed of $1020 \pm 100\,\mathrm{km\,s^{-1}}$ (at an assumed distance of $2.4^{+0.2}_{-0.5}$ kpc; Y. Han et al. 2020, 2025) confirms this discrepancy. A proposed resolution to this is that at least one of the W-R stars in the system has a slow and dense equatorial wind with a fast polar wind, such that the observed slower uniform expansion of the shells and fast winds may coexist. To investigate this we incorporated a phenomenological anisotropic wind into the geometric model that alters the expansion speed and opening angle of some sections of the simulated shell so as to emulate orbital-phase-dependent wind conditions as different latitudes of the W-R stellar surface contribute to the wind–wind shock (Appendix B.4). Such a model cannot rule out or confirm anisotropic winds where the stellar rotation is aligned with orbital motion. However, using this we have found that it is unlikely for the (would-be) anisotropic star to have its rotation significantly misaligned with the orbital plane as we do not find any geometric signatures of this in the nebula. If the slow-wind region extends to high stellar latitudes, we would also not be able to detect such a shell deformation. This is consistent with previous spectroscopic observations of a fast polar wind, given the plane of the orbit is almost in the plane of the sky (inclination of $24° \pm 3°$). Investigating this further with hydrodynamic simulations will be essential to determine if Apep really does harbor a critically rotating star that may be a long gamma-ray burst (LGRB) progenitor.

4.1. Effect on Dust Grains in the Cavity

Our tertiary cone modeling does not exactly produce the observed structure, and one of the last remaining mysteries in the Apep plume geometry is the origin of the horizontal ridge outlining the cavity on its southern border. Our first interpretation of this ridge is that the O star may deflect some proportion of the dust onto this outer ridge, but modeling this has proven difficult. We considered and implemented several models of deflection in an attempt to explain this ridge, where the O star deflects dust particles—into a ring along the entire cavity edge; onto the cavity edge on those angular coordinates colocated with the dust; or onto a central angular position along the cavity boundary with some azimuthal spread—but all three models were unsuccessful in reproducing the geometry. The first two ideas significantly overpredict ridges at other locations that are not seen in the observations, and the third can produce a ridge in the correct location (by design) but at an angle which does not match the observed ridge. Given that this is a persistent feature across the shells, we do not think that this is an anomalous dust feature (created by, e.g., a surface mass eruption). Consequently, our picture of the tertiary shock is that it does not displace dust grains but rather destroys them. Estimates on the dust grain properties within and around the cavity are difficult to discern without spectra, however, but constraints can be inferred based on the environmental conditions.

The disruption of dust grains via radiative torques (radiative torque disruption (RATD)) has recently been studied in the context of W-R CWBs (T. Hoang et al. 2019; R. M. Lau et al. 2023). This occurs due to high-energy photon absorption inducing rotation in asymmetric dust grains, thereby inducing a centrifugal stress which can disrupt the grains (T. Hoang et al. 2019). At a given distance r_* parsecs from a central point source of luminosity L_* (units of $10^9\ L_\odot$) with mean wavelength $\bar{\lambda}_{0.5}$ (in units of 0.5 μm), the maximum size of dust grains with tensile strength S_9 (units of 10^9 erg cm^{-3}) surviving this mechanism is given by T. Hoang et al. (2019) as

$$a_{\mathrm{RATD}} \simeq 0.003197(\bar{\lambda}_{0.5}^{-1.7} L_*^{-1/3} r_*^{2/3} S_9^{1/2})^{1/2.7} \mu\mathrm{m}. \quad (5)$$

Using this, together with our cavity edge distance of 1700 au, a mean wavelength given by a blackbody distribution of 30 kK, a luminosity of $10^{5.9}\ L_\odot$ (typical of O8 Iaf supergiants), and a grain maximum tensile strength of 10^9 erg cm^{-3} (for disordered grains; T. Hoang & L. N. Tram 2019), we obtain a maximum surviving dust grain size of ∼4 nm. The timescale on which this destruction takes place is

$$\tau_{\mathrm{RATD}} \simeq \frac{368}{438}\, \bar{\lambda}_{0.5}^{-1.7} L_*^{-1} r_*^2 S_9^{1/2} (10\, a_{\mathrm{RATD}})^{-0.7}\ \mathrm{yr}, \quad (6)$$

which, with the same parameters and calculated maximum grain size, is ∼6 yr (T. Hoang et al. 2019). More ordered, stronger grains such as graphite can have tensile strengths of $\sim 2 \times 10^{10}$ erg cm^{-3} (T. Hoang & L. N. Tram 2019), however, which results in a maximum grain size of ∼13 nm and a destruction timescale of $\gtrsim$12 yr. We note that the maximum grain sizes and destruction timescales due to the RATD mechanism could be underestimated by factors of a few given our order of magnitude uncertainties in the tensile strengths across the true grain distribution. We also note that these calculations are done given parameters at the periphery of the

dust cavity; in reality, we might expect a gradient of dust conditions across the cavity "surface." These calculations assume that the environmental conditions are constant across the destruction timescale, when this is not the case: the dust shell, produced from the colliding winds of the W-R + W-R binary, is moving radially outwards first into the O star's wind and radiation and then out of it. In parallel the dust is becoming less dense as it expands into a larger shell surface with time, implying that the dust grains will be less shielded from radiation as time goes on (which explains in part why the tertiary star apparently destroys so much dust compared to the similar radiation environment of the central W-R + W-R binary).

Our overall picture of the dust destruction resulting in a circular cavity consists of several processes in parallel. We suggest that the tertiary wind–wind shock breaks down large grains into nanograins via grain–grain and gas–grain collisions, while the radiation pressure from the O supergiant disrupts large grains above ∼4 nm into nanograins via the RATD mechanism. The closest $\lesssim$1700 au to the O tertiary will see an ionizing environment up to orders of magnitude more intense than the photon-dominated regions around sites of massive stellar formation (mainly due to the much smaller length scales involved in the cavity, albeit on shorter timescales), and so nanograins will be photodissociated by the UV flux as they are formed (T. Schirmer et al. 2022). The many competing phenomena warrant the use of detailed simulations, for example with a hydrodynamical code, to model this observed geometry in Apep in future studies.

4.2. Orbit of the Tertiary Star

If we take the distance to the Apep system to be 2.4 kpc (J. R. Callingham et al. 2019; Y. Han et al. 2020), the tertiary star must be presently 1700 ± 200 au from the W-R + W-R binary center of mass. Given the positioning of the dust cavity, the O star is approximately 34° ± 10° above the plane of the W-R + W-R orbit. If the tertiary star is in a circular orbit at such a distance, with a total system mass of $\sim 80\,M_{\odot}$, the orbital period should be of order $P_{\rm tert} \sim 8 \times 10^3$ yr. If this is the case, we would expect the tertiary star—and by extension its associated cavity in the dust plume—to move ∼28° in its orbit around the common center of mass over the three visible dust shells and $3P_{\rm orb} \simeq 600$ yr of visible dust in the JWST imagery. This extent of cavity displacement is not supported by our fits, which is constrained to $\lesssim$10° of movement. Imaging of even older shells—which would be cooler, older, and larger—with the Atacama Large Millimeter Array (ALMA) may unambiguously reveal the movement of this cavity over a longer timescale. Similarly, the detection of molecular lines, and their subsequent radial velocity profile, in the Apep nebula with ALMA would yield an unambiguous expansion velocity (and corresponding orbital period) of the nebula.

The slow movement of the cavity can be explained if the O star companion is on an eccentric orbit, where it is presently near apastron and moving slower relative to an analogous circular orbit. This is a plausible explanation, since often in hierarchical triples the companion star is on a highly elliptical, distant orbit (J. M. O. Antognini & T. A. Thompson 2016; S. Toonen et al. 2016). In such a case, the tertiary star will have a perturbative influence on the dynamics of the inner binary. Even with a modest eccentricity of $e_{\rm tert} = 0.1$, the Kozai–Lidov timescale of this configuration would be of order $P_{\rm KL} \sim 10^5$ yr (J. M. O. Antognini 2015; S. Naoz 2016). Massive stars—which eventually evolve into W-R stars—have lifetimes of a few million years, and so the Apep system will have experienced several Kozai–Lidov timescales at minimum; since this mechanism can in principle pump the eccentricity of the inner binary up to values of $e \gtrsim 0.95$, the companion star must be accounted for in any binary evolution studies of the Apep system in order to discern past epochs of close passages and/or mass transfer.

4.3. Concluding Remarks

The creation and processing of dust grains into the ISM influences all areas of astronomy, and the binary W-R stars together with the dust-destroying O supergiant at the heart of the Apep nebula cements it as a truly unique astrophysical laboratory. The JWST observations of Apep reveal luminous circumstellar dust that is several times the age of that revealed around WR 140 in previous observations (R. M. Lau et al. 2022; E. P. Lieb et al. 2025), and support our finding that the O supergiant "northern companion" is dynamically associated with the binary W-R stars in Apep; this is the first time that dust destruction has been observed by a tertiary star in a colliding wind nebula, and marks Apep as part of a rare class of triple CWBs together with WR 147 (L. F. Rodríguez et al. 2020). Our work motivates more detailed simulations of the dust destruction in such a system, for example with a hydrodynamic code, and the modeling of dynamical effects of a tertiary star on the binary evolution in W-R CWBs.

Acknowledgments

We are grateful to Peredur Williams, Orsola De Marco, and Katelyn Smith for valuable discussions during the analysis and writing of this work. We thank the University of Sydney and University of Queensland "FOCI" group for helpful discussions and feedback throughout the project. R.M.T.W. acknowledges the financial support of the Andy Thomas Space Foundation. S.D. and B.J.S.P. were funded by the Australian Government through the Australian Research Council DECRA fellowship DE210101639. N.D.R. is grateful for support from the Cottrell Scholar Award #CS-CSA-2023-143 sponsored by the Research Corporation for Science Advancement.

This work is based on observations made with the NASA/ESA/CSA James Webb Space Telescope. The data were obtained from the Mikulski Archive for Space Telescopes at the Space Telescope Science Institute, which is operated by the Association of Universities for Research in Astronomy, Inc., under NASA contract NAS 5-03127 for JWST. These observations are associated with Program ID 5842. Support for Program ID 5842 was provided by NASA through a grant from the Space Telescope Science Institute, which is operated by the Association of Universities for Research in Astronomy, Inc., under NASA contract NAS 5-03127.

We acknowledge and pay respect to the traditional owners of the land on which the University of Queensland is situated, upon whose unceded, sovereign, ancestral lands we work. We acknowledge the traditional custodians of the Macquarie University land, the Wallumattagal clan of the Dharug nation, whose cultures and customs have nurtured and continue to

nurture this land since the Dreamtime. We acknowledge the tradition of custodianship and law of the Country on which the University of Sydney campuses stand. We pay our respects to those who have cared and continue to care for Country.

Author Contributions

R.M.T.W. developed the geometric wind model, conducted all data analysis, and led the writing of the manuscript. Y.H. led the telescope proposals and contributed to discussions and analysis. B.J.S.P. and P.G.T. supervised the project and provided comments on the manuscript. S.D. and B.J.S.P. reduced and processed MIRI imagery for both scientific and esthetic purposes. All authors contributed to the text of the final manuscript.

Code Availability

The geometric model code, `xenomorph` (R. M. T. White 2025), is open source on GitHub and available at github.com/ryanwhite1/xenomorph, with a documentation site online at ryanwhite1.github.io/xenomorph/. We encourage community contributions to the code through pull requests, and any suggestions or feedback on the state of documentation. The code makes use of JAX (J. Bradbury et al. 2018), `Numpy` (C. R. Harris et al. 2020), `Matplotlib` (J. D. Hunter 2007), `Scipy` (P. Virtanen et al. 2020), and `Astropy` (Astropy Collaboration et al. 2013, 2018, 2022). The version of the code current to the date of publication is available on Zenodo and can be accessed via doi:10.5281/zenodo.15875502.

Data Availability

The JWST data used in this study were obtained from the Mikulski Archive for Space Telescopes (MAST; https://archive.stsci.edu/missions-and-data/jwst) at the Space Telescope Science Institute, under JWST GO Program ID 5842. The JWST data used in this paper can be found in MAST: doi:10.17909/mf14-ga19.

Facilities: JWST (MIRI), VLT:Melipal (VISIR).

Appendix A
Image Data Processing

A.1. For the Poster Image

We use the software Pixinsight[10] for the generation of the image shown in Figure 1, aimed at generating a false-color composite image for visual recognition of the shell structures and other features in the image. We start by cropping the image and filling in parts of the image missing data by interpolation with surrounding pixels. We then construct the false-color composite by assigning the channels red, green, and blue, respectively to F2550, $0.5 \times$ F770 $+ 0.5 \times$ F1500, and F770. A rectangular segment containing little dust or stars is set as a background reference and the colors are transformed such that this is set to a neutral gray color tone. We then apply a custom nonlinearization to the image to reveal the background shells, and increase the color saturation. Lastly, we use the Python package starnet++,[11] a neural-network-based tool to mask the stars and apply a custom color transformation to get closer to the appearance of a blackbody. We emphasize that the aim of these processes is for aesthetic and visual purposes rather than scientific.

A.2. For Geometric Fitting

The fitting of geometric forms to data relies primarily on the alignment of ridges present in both the model image and the observed data. Therefore, we minimally processed the raw VISIR and MIRI data to accentuate the ridge geometry. To do this we performed a 64th percentile background subtraction on each image then normalized all pixel values to be between zero and one (by taking a floor of zero brightness and then dividing by the maximum value). We then raised all pixel values to the 0.5th power, which emphasized the nebula brightness' suitably for fitting. The reference images in Figure 2 (shown by the blue shading) have been processed in this way.

Appendix B
The `xenomorph` Geometric Model

The basic idea that underpins the geometric model is to approximate instantaneous dust production within the wind collision region as a ring expanding from the stagnation point down the surface of the wind–wind shock cone. This ring is initialized in the orbital plane at the location of the "secondary" star (in terms of wind strength, not mass as is convention), and ejected along the line of sight from the primary star to the secondary at the wind speed of the primary. As the two stars orbit each other, the direction of ring ejection changes with the result that the plume "wraps" to create the characteristic spiral. This is illustrated in Figure 4.

Even at this basic level, the model has a multitude of parameters that can be changed at run time. The parameters most fundamental to this geometric approximation are the number of discretized points within each ring, and the number of rings to be produced over the course of one orbital period. Ideally both of these would be as large as possible in order to reduce the error associated with approximating a continuous process as discrete (so-called quantization error); practically we usually set these to be 400 points per ring and 1000 rings per orbit, which provide a dense point cloud for the nebula.

To render the point cloud into an image that resembles the real nebula, we take a histogram of the line-of-sight projection of the cloud. Even though these nebulae are 3D, in imaging we observe the column density of the dust due to its projection onto the plane of the sky. Hence by collapsing our modeled 3D

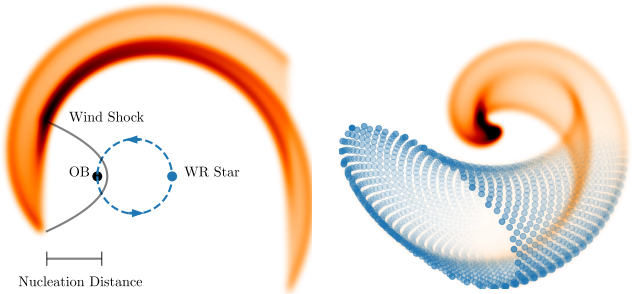

Figure 4. The idea for the geometric model is to initialize a ring of points around the wind–wind shock at some nucleation distance behind the secondary star (usually an OB-type star). As the binary orbits the common center of mass, the formed dust (and discretized rings/particles in the right figure) gets wrapped into a spiral as it expands out from the central source. Note that there are orders of magnitude fewer particles (compared to the default code setting) in the right-side plot for visualization purposes.

[10] https://pixinsight.com/
[11] https://www.starnetastro.com/

point cloud to a 2D image we can reproduce the observed images. By utilizing the weighting functionality of histograms, we can selectively alter the importance of selected points in order to emulate physical phenomena responsible for sculpting the nebula (e.g., dust turn-off, azimuthal variation, etc.).

Previous geometric models have been successful in reproducing the structure of the spiral nebula, although they are computationally inefficient. If parameter inference is the goal of using these models, we need to make the model as computationally fast as possible so as to reduce the computation time, both for interactive fitting and particularly to enable machine optimization with an MCMC. Further, the high dimensionality of these problems requires that gradient-based, HMC methods be used so that the model can converge to a valid solution in a finite time. Fortunately, the JAX Python framework (J. Bradbury et al. 2018) offers automatic differentiation capability for Python codes and comes standard with "Just In Time" compilation that speeds up model evaluation significantly. Therefore, creating a geometric model from scratch with JAX allows us to satisfy all needed criteria at once. Indeed, our complete code takes of order $\lesssim$0.1 s to generate the hundreds of thousands of particles in the point cloud and render them into an image, compared to that of $\sim$5 s with an equivalent implementation in stock `Numpy` (C. R. Harris et al. 2020).

B.1. The Basic Ring Model

Before rings can be created, we first need a model of the binary orbit so that we know where to initialize the rings and in what direction they move. The motion of two celestial bodies in their mutual orbit is described by Kepler's equation (see C. D. Murray & S. F. Dermott 1999, for a review of the two-body problem). To calculate the true anomaly of a star at any point over the orbital period (i.e., with known mean anomaly, M), Kepler's equation

$$M = E - e \sin E, \tag{B1}$$

must be solved for the eccentric anomaly, E. Traditionally, this is solved by an iterative method which converges to the correct value of E given M. Those iterative methods are not differentiable, however, and so we use the noniterative method described in F. L. Markley (1995) and implemented in JAX in S. Hattori et al. (2024). From the eccentric anomaly, we can then calculate the true anomaly, ν, analytically via

$$\nu = 2\ \mathrm{atan2}(\sqrt{1+e}\sin(E/2), \quad \sqrt{1-e}\cos(E/2)). \tag{B2}$$

Since the mean anomaly changes linearly with time, this calculation of true anomaly provides the angular position of each body relative to the focus of their orbits (i.e., the center of mass) at constant time intervals.

The choice of the mean anomaly grid is directly proportional to the time domain over which dust is produced. If the system in question produces dust constantly, a grid choice encompassing $0 \leqslant M \leqslant 2\pi$ then results in the relevant true anomalies with which to initialize rings. If the system is an episodic dust producer, i.e., produces dust between a well-defined dust "turn-on" and "turn-off," the choice of the mean anomaly grid is not so straightforward. Previous implementations of the geometric model would initialize rings over a full circle of mean anomaly but then discard rings whose true anomaly fall out of the specified turn-on/off range. As producing "invisible" rings requires significant computational work—the same computation time as the visible rings, but with no effect on the visible nebula—we avoid this and devise a method to produce only rings that contribute to the visible spiral plume.

To produce rings only between dust turn-on/off, we need to find a grid of mean anomalies between our true anomaly bounds; essentially the inverse problem to that described above. We begin with our true anomaly bounds, ν_{t_on} and ν_{t_off}. For the true anomaly we follow the convention that periastron corresponds to $\nu = 0$ and so we expect that the turn-on is in the range $-\pi \leqslant \nu_{t_\mathrm{on}} \leqslant 0$ radians; conversely $0 \leqslant \nu_{t_\mathrm{off}} \leqslant \pi$ radians for the turn-off anomaly. The eccentric anomaly corresponding to dust turn-on is then calculated as

$$E_{t_\mathrm{on}} = 2\ \mathrm{atan2}\left(\tan\left(\frac{\nu_{t_\mathrm{on}}}{2}\right), \sqrt{\frac{1+e}{1-e}}\right), \tag{B3}$$

and the same is used to calculate E_{t_off} instead with ν_{t_off}. The result of this can be substituted into Equation (B1) to then obtain the mean anomaly bounds corresponding to dust turn-on/off, $M_{t_\mathrm{on/off}}$. For the episodic dust producers, we create a grid of mean anomalies in the range $M_{t_\mathrm{on}} \leqslant M \leqslant M_{t_\mathrm{off}}$ for each single shell, which is fed back into the solver to find the true anomalies corresponding to the stellar orbits.

In order to eventually determine the size and distance of each ring from the binary center, the age of each ring must be calculated. An equally spaced grid within the mean anomaly bounds naturally provides an equally spaced grid in time. The age of the ring corresponding to each mean anomaly value, relative to the orbital period (i.e., in the range $0 \leqslant t_{\mathrm{age}} \leqslant 1$), which can then be calculated by

$$t_{\mathrm{age}} = \mathrm{mod}\left(\frac{\mathrm{mod}\ (M, 2\pi)}{2\pi} - \phi, 1\right), \tag{B4}$$

where ϕ is the current orbital phase of the binary. Equation (B4) results in rings created at the current orbital phase having the lowest age, and those at the previous mean anomaly grid position having the largest age. When multiple shells of material are being simulated, the grids of mean anomalies and ages are tiled N_{shell} times, where each successive tiling adds an additional $+1$ to the age, which accounts for the previous orbital periods of time. To convert from this nondimensionalized age relative to the orbital period into an absolute time, we can simply multiply by P_{orb}.

Using the true anomalies corresponding to dust production, the positions of the stars in their orbits can be calculated so that the position and orientation of each ring can be found. The nondimensionalized position of the primary star is calculated as

$$\hat{\boldsymbol{r}}_1 = (\cos(\nu), \sin(\nu), 0), \tag{B5}$$

for each true anomaly value, where we note that we take the orbital motion to be in the x–y plane; the corresponding position of the secondary is just the negative of Equation (B5), $\hat{\boldsymbol{r}}_2 = -\hat{\boldsymbol{r}}_1$, since angular displacement of the stars is always π radians relative to the system barycenter. To convert this into a true distance, we multiply by the distance of each star relative to the system barycenter, $\overrightarrow{r_{1/2}} = r_{1/2}\,\hat{\mathbf{r}}_{1/2}$, where

$$r_{1/2} = a_{1/2}(1 - e\cos(E)), \tag{B6}$$

for each corresponding eccentric anomaly to the true anomaly, and for each star. From Kepler's third law, the semimajor axis

of the binary system is

$$a = \left(\frac{G(M_1 + M_2)P_{\rm orb}^2}{4\pi^2} \right)^{1/3}, \tag{B7}$$

and so the semimajor axis of each star in their orbits relative to the system barycenter is

$$a_1 = a\,\frac{M_2}{M_1 + M_2},\ a_2 = a\,\frac{M_1}{M_1 + M_2}. \tag{B8}$$

Calculating the absolute positions of the stars, especially relative to each other, is necessary when determining the position and angle of each ring relative to the system.

We construct the rings along the x-axis (so that a circle is seen in the $y-z$ plane), and populate them with $N_{\rm particles}$ particles per ring; this means that there are a total of $N = N_{\rm rings} \times N_{\rm particles}$ particles in the "point cloud" of each nebula shell. The particles are linearly spaced within the ring and constitute a full circle, such that $0 \leqslant \theta_{\rm particle} \leqslant 2\pi$. The coordinates of the particles within each ring depends on the plume opening angle, $\theta_{\rm OA}$, by

$$\begin{aligned} \hat{\boldsymbol{r}}_{\rm particle} = \Bigg(& \cos\left(\frac{\theta_{\rm OA}}{2}\right), \\ & \sin\left(\frac{\theta_{\rm OA}}{2}\right)\sin(\theta_{\rm particle}), \\ & \sin\left(\frac{\theta_{\rm OA}}{2}\right)\cos(\theta_{\rm particle})\Bigg). \end{aligned} \tag{B9}$$

The particle coordinates within each ring are then scaled by the distance they should have traveled given the ring age and the W-R dust expansion speed:

$$\boldsymbol{r}_{\rm particle} = v_{\rm dust}\ t_{\rm age}\ \hat{\boldsymbol{r}}_{\rm particle}. \tag{B10}$$

This expands the ring along the surface of a cone projecting outwards from the system center, and both enlarges the ring and displaces it by the appropriate amounts. The direction that this cone is facing is calculated from the current stellar positions as

$$\varphi = \mathrm{atan2}\left(\frac{y_2 - y_1}{||\overrightarrow{r_1} - \overrightarrow{r_2}||},\quad \frac{x_2 - x_1}{||\overrightarrow{r_1} - \overrightarrow{r_2}||} \right), \tag{B11}$$

which is the angle from the primary to secondary star in the orbital plane. Since the rings are created along the x-axis, they must be rotated about the z-axis by φ so that they align with the direction vector of the primary to the secondary. That is, we update each particle vector to be

$$\begin{aligned} \boldsymbol{r}_{\rm particle} &= (R_z(\varphi)\boldsymbol{r}_{\rm particle}^T)^T \\ &= \left(\begin{bmatrix} \cos(\varphi) & -\sin(\varphi) & 0 \\ \sin(\varphi) & \cos(\varphi) & 0 \\ 0 & 0 & 1 \end{bmatrix} \begin{bmatrix} x_{\rm particle} \\ y_{\rm particle} \\ z_{\rm particle} \end{bmatrix} \right)^T. \end{aligned} \tag{B12}$$

While Equations (B9)–(B12) are described in terms of a single particle, these operations are applied to all of the particles that belong to a single ring at once. This procedure is made computationally efficient by the `vmap` functionality within JAX, which automatically vectorizes the particle and ring mathematics.

In our simulations we create each ring with $N_{\rm particles} = 500$ particles and each shell with $N_{\rm rings} = 1000$ rings. These numbers were chosen as a suitable middle ground between computational performance (which would favor fewer rings and particles) and dense spatial sampling of the plume (which would require as many rings and particles as possible). Since true colliding wind nebulae are smooth to first order, our approximation of a point cloud introduces a quantization error into any rendered image. Hence, our choice of $N_{\rm particles}$ and $N_{\rm rings}$ was motivated so that there would always be a small but nonzero number of particles in even the lowest-density rendered pixels.

With our point cloud generated, next we need to render an image of the simulated nebula so as to compare it to observations. For this, we collapse our 3D point cloud into 2D, which is analogous to its projection in the plane of the sky. We then take a 2D histogram of these collapsed particle locations, which produces a "heat map" of the nebula. Although this is a simple procedure, producing a column density of particles in this way is essentially what we observe when taking real astronomical images of optically thin material: the line-of-sight projection of material in the field of view. As a by-product, using a histogram allows us to very easily change the number of bins in the render as a proxy of changing the angular resolution of the simulation. This proves useful when comparing a simulated image to that taken by a telescope: we can render the image with the exact number of pixels (bins) needed on the correct angular pixel scale by manually fixing just two parameters.

Since the image is rendered in 2D, we must first ensure that the plume geometry is consistent with the orbital elements prior to rendering. That is, we must rotate the entire point cloud in 3D with the appropriate Euler angles so that the point cloud resembles the true geometry from our (observer's) perspective. We update the coordinates of each particle within the point cloud, $\boldsymbol{r}_{\rm particle}$, as

$$\overrightarrow{r}_{\rm particle} = (R_z(-\Omega)R_x(-i)R_z(-\omega)\,\overrightarrow{r}_{\rm particle}^{\,T})^T, \tag{B13}$$

where Ω is the binary orbit longitude of ascending node, i is the inclination, and ω is the argument of periastron. Note that these parameters do not affect the intrinsic geometry of the nebula, but only its projection into the plane of the sky.

B.2. Azimuthal and Orbital Variation in Dust Production

The first additional feature to the model that we consider is the azimuthal variation in dust production on each created ring. WR 140 was observed to create dust most strongly on the trailing edge (with respect to the orbital motion) of its shock cone in P. M. Williams et al. (2009a). In the time since, this phenomenon has been required to reproduce the observed geometry of WR 140 in multiepoch imaging, including with JWST (P. M. Williams et al. 2009a; Y. Han et al. 2022; R. M. Lau et al. 2022; E. P. Lieb et al. 2025). This enhanced dust production along the trailing edge of the shock has also been supported by hydrodynamical simulations of WR 104 (A. Lamberts et al. 2012; A. Soulain et al. 2023), and also more generally in the case of CWBs on eccentric orbits with nonequal winds (M. N. Lemaster et al. 2007).

Since we render each point cloud into an image via a histogram, we can apply weightings to each particle, which affects how much it contributes to the final geometry. Utilizing

this functionality, we model this azimuthal variation as a Gaussian function multiplier applied to each particle within a ring and each entire ring respectively, similarly to Y. Han et al. (2022). That is, the weighting factor of each particle from azimuthal variation is calculated by

$$\delta w_{\rm az} = \max\left\{1 - (1 - A_{\rm az})\exp\left(-\frac{(\theta_{\rm particle} - \theta_{\rm az_min})^2}{2\sigma_{\rm az}^2}\right),\ 0\right\}, \tag{B14}$$

where $A_{\rm az}$ is the global strength of the variation, $\theta_{\rm particle}$ is the angular coordinate of the particle within the ring (0° being in the $+z$-direction), $\theta_{\rm az_min}$ is the location of the azimuthal minimum, and $\sigma_{\rm az}$ is the spread of the variation across the angular coordinates of the particles. Although each of these are free parameters, we usually set $\theta_{\rm az_min} = 90°$ in practice; this corresponds to the leading edge of the dust plume with respect to the orbital motion resulting in dust production being weaker at the leading edge. A minimum value of zero in Equation (B14) is enforced since $A_{\rm az}$ can in principle take any positive value, although it is usually in the range $0 \lesssim A_{\rm az} \leqslant 1$. This multiplicative factor calculated for all of the particles within the ring, and we approximate this effect as being constant across orbital phases.

The dust nebula of WR 140 shows evidence not only of azimuthal asymmetry, but orbital modulation in dust production between the classical turn-on and -off (P. M. Williams et al. 2009a; Y. Han et al. 2022). This manifests as a dip in the dust production when the binary stars are near periastron, which results in two distinct phases of dust nucleation per orbit: at ingress and egress. We model this orbital modulation much in the same way as for the azimuthal variation:

$$\delta w_{\rm orb} = \max\left\{1 - (1 - A_{\rm orb})\exp\left(-\frac{(\nu_{\rm ring} - \nu_{\rm orb_min})^2}{2\sigma_{\rm orb}^2}\right),\ 0\right\}, \tag{B15}$$

which is applied to an entire ring's weighting. The parameters in this Gaussian are analogous to that of the azimuthal variation, instead using the true anomaly of the entire ring instead of a particle angular coordinate, and with orbital variation amplitudes and spreads instead of azimuthal. Although technically free, we set $\nu_{\rm orb_min} = 180°$, corresponding to the periastron of the orbit where the dust production may be weak during the dust production phase.

For those systems that do not show signs of azimuthal and/or orbital variation, we may simply set $A_{\rm az} = A_{\rm orb} = 1$ in Equations (B14) and (B15), thereby setting the weighting effect to zero. We show in Figure 5 these weighting values given the particle angle or ring true anomaly for multiple values of A and σ.

When the true anomaly at the current orbital position falls between that of the turn-on and -off threshold values, the produced rings contribute to the visible dust plume. We should not expect, however, that the turn-on or -off of dust production is instantaneous, but rather that there is a gradual change in the production rate. Hence as an additional feature, we have implemented a turn-on/off smoothing in the dust production that was not present in previous versions of the geometric model. To do this, we use a half-Gaussian function to decrease the weights of rings that are outside of the usual dust

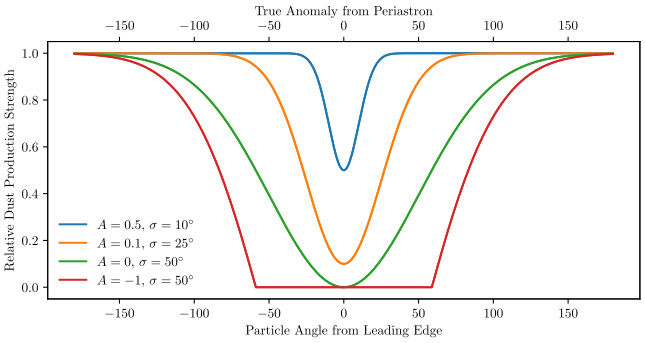

Figure 5. The free parameters of Equations (B14) and (B15) change the depth and breadth of the strength variations in dust production. The top axis represents the weighting applied to each ring as a function of true anomaly for a representative set of free parameters, while the bottom axis represents the weighting applied to each particle within each single ring.

production regime; this function has a value of one at the usual dust production true anomaly bounds, and decreases with standard deviation $\sigma_{\rm gradual}$ outside of the usual dust production regime. To include this we therefore have to inject some rings outside of the usual dust production true anomaly bounds, $\nu_{t_{\rm on/off}}$. We modify the previous bounds to now be

$$\begin{aligned} \nu_{t_{\rm on}} &= \max\{-180°,\ \nu_{t_{\rm on}} - 2\sigma_{\rm gradual}\}, \\ \nu_{t_{\rm off}} &= \min\{180°,\ \nu_{t_{\rm off}} + 2\sigma_{\rm gradual}\}, \end{aligned} \tag{B16}$$

where we include rings up to two standard deviations outside of the usual bounds. For each ring, we then apply a histogram weighting of

$$\delta w_{\rm gradual} = \begin{cases} \exp\left(\dfrac{(\nu_{\rm ring} - \nu_{t_{\rm on}})^2}{2\sigma_{\rm gradual}^2}\right) & \nu_{\rm ring} < \nu_{t_{\rm on}}, \\ 1 & \nu_{t_{\rm on}} \leqslant \nu_{\rm ring} \leqslant \nu_{t_{\rm off}}, \\ \exp\left(\dfrac{(\nu_{\rm ring} - \nu_{t_{\rm off}})^2}{2\sigma_{\rm gradual}^2}\right) & \nu_{t_{\rm off}} < \nu_{\rm ring}, \end{cases} \tag{B17}$$

to emulate a gradual dust production turn-on and -off. With this as the final required weighting factor, the overall weighting on each particle in the point cloud is calculated as

$$w = \delta w_{\rm az} \times \delta w_{\rm orb} \times \delta w_{\rm gradual}. \tag{B18}$$

The effect of each of these variations on the nebula plume is shown in Figure 6. For the Apep system in particular, we make more modifications to the total weighting of each particle, which we discuss in Appendix B.6.

B.3. Acceleration in the Dust Shell

W-R stars are among the most luminous stellar objects, and so the environment immediately surrounding them is engulfed in intense radiation. The winds of these stars are known to accelerate to a terminal velocity some time after leaving the photosphere of the star because of the intense radiation pressure from the stars themselves (D. C. Abbott 1978). Further downstream, we should expect that the dust grains formed would experience intense radiation pressure given that W-R stars are at a significant fraction of their Eddington

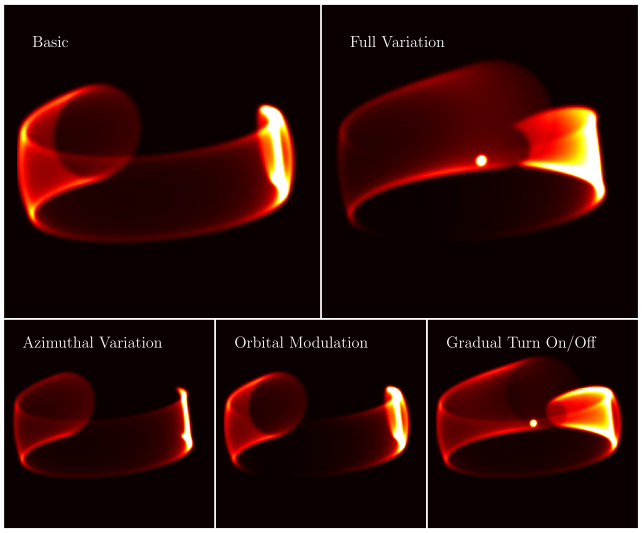

Figure 6. Each higher-order variation affects the dust plume in different ways. The top right plot shows how an arbitrary test system appears with only the "basic" model implementation as described in Appendix B.1. The bottom row shows each of the higher-order dust production variations discussed so far, and their effect on the "basic" plume in isolation. The top right plot shows the effect of including all of these features at once. The value of each effect in the figure is $\sigma_{az} = 60°$, $A_{az} = -1$, $\sigma_{orb} = 40°$, $A_{orb} = 0$, and $\sigma_{gradual} = 19°$.

luminosity (G. Gräfener et al. 2011; A. Maeder et al. 2012). This radiation pressure has been observed accelerating gas around clusters of stars (N. Murray et al. 2011), and has been used to explain the apparent acceleration of dust shells around WR 140 (Y. Han et al. 2022).

In the paper describing the radiative acceleration of dust around WR 140, the authors do not explicitly include acceleration into their geometric model. For the first time, we include this acceleration in our model. Y. Han et al. (2022) propose an acceleration model that is largely physically motivated: the dust nucleates at some distance from the star in an optically thick regime while accelerating at a constant rate, then becomes optically thin some time later and proceeds to accelerate at a decreasing rate. The strength of acceleration in this model is parameterized by radial distance from the central W-R + O binary, as one would expect from radiation pressure which follows an inverse-square law. Unfortunately elements of this prescription are difficult to integrate into our geometric model; the ejected rings are parameterized mainly by their age, which is subsequently used to calculate their (nonaccelerated) radial distance. In order to incorporate the acceleration terms from Y. Han et al. (2022) into our geometric model, an iterative method would be required to find the correct accelerated distance. This introduces computational complexity and is at odds with gradient computation in JAX.

To maximize computational efficiency and maintain gradient calculations, we instead use a phenomenological model for acceleration parameterized by the dust ring age: the velocity of each ring is the exponential decay of some initial velocity v_i to a terminal velocity v_∞ in the radial direction from the central W-R binary. That is:

$$v(t_{age}) = v_\infty + (v_i - v_\infty)\exp(-10^{\mathcal{A}}\, t_{age}), \tag{B19}$$

where $\mathcal{A}$ is a scaling constant which determines the slope of the exponential (i.e., the strength of the acceleration). When v is in units of kilometers per second and t_{age} is in units of years, we find this exponential constant should be roughly in the range 10^{-5}–10^{0} yr^{-1}, or $-5 \lesssim \mathcal{A} \lesssim 0$.

Including this acceleration into the model means that we replace the v_{dust} parameter in Equation (B10) so that the equation now reads

$$\boldsymbol{r}_{particle} = v(t_{age})\, t_{age}\, \hat{\boldsymbol{r}}_{particle}. \tag{B20}$$

In modeling acceleration this way, we note that we can also easily simulate dust deceleration as needed. In Equation (B19) we see that when $v_\infty < v_i$, the rings are decelerating toward a terminal velocity; conversely, $v_\infty > v_i$ results in dust ring acceleration as we would model in WR 140, for example. The detailed consequences of modeling acceleration with an exponential instead of a power law have not been exhaustively explored. However the acceleration term is dominant only at early orbital phases when the dust is close to the luminous stars. At present there does not exist a large body of observations of CWB systems at these phases, making comparison difficult. Since Y. Han et al. (2022) and our implementation of acceleration both yield velocity converging to a terminal value, we expect that any difference in geometric fits would be small and not the dominant source of model error.

B.4. Modeling Wind Anisotropy

One of the biggest unanswered questions about W-R CWBs is whether their spiral nebulae can exhibit evidence of wind anisotropy, particularly in the case of the Apep system (J. R. Callingham et al. 2019). The dominant wind in the Apep system has been suggested as being anisotropic on account of the large discrepancy between the polar wind speed (measured through spectroscopy) and the nebula expansion speed (measured kinematically); the idea here is that the WC star in Apep may harbor a slow, but dense equatorial wind, which is responsible for the visible dust plume as well as a fast and sparse polar wind. This interpretation suggests that this star is critically rotating, in which case Apep is the most likely LGRB progenitor candidate known in our Galaxy. It is therefore essential to look for any evidence of wind anisotropy in the visible plume to investigate this hypothesis.

We present here the first attempt at integrating an anisotropic wind into the geometric model for W-R CWBs. Evidence of anisotropy in the dust plume may be present if the star with the higher-momentum wind is inclined with respect to the orbital plane of the binary; this would mean that the wind at the shock interface would change in momentum depending on the orbital positions of the stars. The inclination of this star may also be misaligned with the argument of periastron of the orbit, ω, which would affect the anisotropy–true anomaly correlation. These ideas are shown in Figure 7.

We parameterize the strength of wind anisotropy based on the origin latitude of the wind that is currently causing the colliding wind shock, ϑ. We take $\vartheta = 0$ as being along the equator of the windy star, and so the value of ϑ at any point along the orbit is calculated as

$$\vartheta(\nu) = |\iota \sin(\nu - \varpi)|, \tag{B21}$$

where ι is the inclination of the star with respect to the orbital plane, and ϖ is the argument of periastron offset; the absolute value assumes that the wind anisotropy is symmetric about the equator.

Figure 7. Wind anisotropies may be visible in the dust plume if the wind-dominant star is inclined with respect to the orbital plane (left). In principle, the axis of rotation could also be misaligned from the periapsis of orbit (right), which might affect the wind anisotropy evidence in elliptical orbits. We have an image available online that shows the effect of a modest (∼30°) spin–orbit misalignment with a faster polar wind.

We expect that a wind anisotropy would manifest itself as a true anomaly dependence on the plume opening angle and/or expansion velocity in the CWB nebula. This is because if the mass loss or speed is latitude dependent, the momentum ratio of the winds at the shock interface would change depending on the wind origin and hence the plume geometry should change as a result. We considered implementing a model in which the rings were elliptical (as opposed to circular), but the WC star is always such a distance from the two stars that the local wind field is essentially planar.

Without detailed knowledge of the exact 3D wind fields around these WC/WN stars, we phenomenologically model these opening angle and expansion velocity perturbations due to anisotropy as multipliers onto the standard parameters, much in the same way we modeled azimuthal and orbital variations as histogram weighting multipliers. These multipliers are

$$\delta v(\vartheta) = 1 + \left(\frac{v_{\text{polar}}}{v(t_{\text{age}})} - 1\right)\tanh\left(10^{m_v}\vartheta^{p_v}\right), \tag{B22}$$

$$\delta\theta_{\text{OA}}(\vartheta) = 1 + \left(\frac{\theta_{\text{OA, polar}}}{\theta_{\text{OA}}} - 1\right)\tanh\left(10^{m_{\text{OA}}}\vartheta^{p_{\text{OA}}}\right), \tag{B23}$$

where we have three additional parameters for each of the velocity and opening angle multipliers; a parameter with the subscript "polar" denotes the value of that parameter due to the polar wind, m_v and m_{OA} represent the value of a constant multiplier onto the latitude dependence of the wind, and p_v/p_{OA} impose a power-law dependence of the anisotropy strength onto the latitude. The tanh function was used here as this allows us to sensitively change the slope and shape of the multiplier dependence on ϕ. As a caveat, this manifests only as a monotonically changing multiplier value and cannot represent a latitude dependence with turning points. This nonmonotonic behavior has been seen in some numerical models of massive stellar winds (B. Hastings et al. 2023), although it is common to assume smoothly changing monotonic wind parameters versus latitude for evolved massive stars (A. J. van Marle et al. 2008). The true W-R wind morphology, including the effects of rotation, would require detailed stellar evolution and magnetohydrodynamical models, and this does not appear to have been published in the literature (although this has been recently done for nonrotating W-R stars in N. Moens et al. 2022).

B.5. Miscellaneous Features and Details

There exist a number of features we have implemented into the geometric model that have either little or no effect on the physical geometry. In the aim of performing statistical inference with our model, we have added in two parameters that affect only the pixel values of the final render: the first is a brightness ceiling on the rendered array as an emulation for image pixel saturation, and the second is a power-law scaling of the remaining pixels mainly to exaggerate otherwise dim pixels. Allowing for these parameters to change makes it easier to compare simulated images to real data, and may allow for faster convergence in statistical methods on our simulations.

The next modification made to the geometric model pertains to the azimuthal angles of particles within each generated ring. Equation (B9) describes the initial Cartesian coordinates of particles within each ring, parameterized by some azimuthal angle θ_{particle} unique to each particle within the ring. In early versions of our model, the grid of these azimuthal angles for particles within each ring was identical across all of the rings in the plume; what we saw was that this accentuated the quantization error of approximating these continuous rings as a series of particles. Since the particles were at identical angular positions within neighboring rings, "stripes" of nebulosity would be visible in the final image. One solution to this would be to simply increase the number of particles in each ring, although this would correspondingly increase the computation time. To minimize this effect, we instead shift the angular coordinate of all particles within a ring by 1 radian across each consecutive ring created. This imposes some quasi randomness in the positions of the particles across neighboring rings, especially since the angular coordinates are modulo 2π.

Since we calculate the position of each star at all times in the model, it is relatively straightforward to take this position and plot the stars on the final rendered image. To do this, we generate the simulated image of the colliding wind nebula, then inject Gaussian flux profiles on the angular positions of the stars at that epoch. The user can determine the amplitude of the flux (how bright the star is), as well as the standard deviation of the flux profile (how much the flux bleeds into neighboring pixels). Including the stars in each image helps to anchor the geometry of the plume with respect to its origin, and the positions of stars become particularly important in our discussion in Appendix B.6.

The final small addition to the geometric model that we describe is the dust nucleation distance. Dust is expected to nucleate at some distance, r_{nuc}, behind the colliding wind shock (referred to as "dust-forming separation" in J. W. Eatson et al. 2022b, for example) where the conditions are favorable.

This nucleation distance is estimated to be typically on the order of tens of astronomical units for W-R CWBs, sufficiently far downstream for both mixing of the two winds and attenuation of the stars' ionizing radiation. Because this nucleation distance is relatively small, the gaps in the models due to dust not yet nucleated are limited to phases close to periastron for the episodic dust producers. To account for this nucleation distance in the model, we include another ring weighting multiplier in the form of a Heaviside step function:

$$\delta w_{\rm nuc} = \begin{cases} 1 & \|\boldsymbol{r}_{\rm particle}\| \geqslant r_{\rm nuc}, \\ 0 & \text{otherwise}, \end{cases} \tag{B24}$$

which is then included in Equation (B18). Including this feature mainly results in a delay in dust production from the orbital motions of the stars, and has no impact on dust shells that are not actively forming dust. The strongest evidence for delayed onset of dust formation, apart from in hydrodynamical simulations, comes from CWB light curves where phase shifts between orbital data and infrared peaks are apparent.

B.6. Modeling of Effects from a Tertiary Companion

Previous models of Apep have been successful in reproducing most but not all of the geometry of the colliding wind nebula. In particular, the northern region of the VISIR image pane of Figure 3 is not suitably reproduced by previous versions of the geometric code (see the top panel of Figure 3 for a representative example of previous attempts). Upon realizing that the cavity in the plume aligned perfectly with the apparent position of the northern companion of Apep's inner binary, we began investigating how a distant third massive companion could influence a colliding wind nebula. The dominant effect appears to be the destruction of the already formed dust once it collides with the tertiary O star wind. With this in mind, our model "destroys" dust that falls within some angular distance of the tertiary star with respect to the inner W-R + W-R binary.

Like the generation of the colliding wind nebula, the cavity region predominantly relies on a few key parameters: the position of the tertiary star with respect to the inner binary and the cone opening angle of the cavity. For the former, in the code we define the position of the third star in spherical coordinates with respect to the inner binary orbital plane. That is, we choose the angular location of the cavity with a polar and azimuthal angle, $\beta_{\rm tert}$ and $\alpha_{\rm tert}$, as well as the radial distance of the third star, $r_{\rm tert}$.

With these parameters, we de-weight the generated points whose angular coordinates are close enough to the center of the cone projection axis. To calculate the angular distance, we use the formula from L. M. Kells & W. F. Kern (1940), modified to fit with the convention that the inclination $\theta = 0$ is at the north pole rather than $\theta = -\pi/2$:

$$\begin{aligned} \Theta = \arccos[&\cos(\beta_{\rm tert})\cos(\beta_{\rm part}) \\ &+ \sin(\beta_{\rm tert})\sin(\beta_{\rm part})\cos(\alpha_{\rm tert} - \alpha_{\rm part})]. \end{aligned} \tag{B25}$$

We then change the weighting of each point in the rendered image by a Gaussian according to their angular distance from the projected cone:

$$\delta w_{\rm tert} = 1 - A_{\rm tert} \exp\left(-\frac{2\Theta^2}{\theta^2_{\rm OA,tert}}\right), \tag{B26}$$

where $A_{\rm tert}$ is the amplitude of the dust destruction, Θ is the angular distance for each particle from the center of the cone, and $\theta_{\rm OA,tert}$ is the cavity opening angle. This is then appended onto Equation (B18) as another preprocessing step onto the final rendered plume. Rather than setting $\delta w_{\rm tert} = 0$ for all particles with $\Theta < \theta_{\rm OA,tert}$ we chose to model this effect with a Gaussian falloff; we would expect that all dust particles having a trajectory that impacts the tertiary O star should be destroyed, but as their impact parameter gets smaller (that is, as their trajectory deviates further from the tertiary star's position) we expect that proportionally fewer dust grains will be destroyed. As shown in Figure 2 (which includes the destruction effect with parameters as in Table 2), this reproduces the geometry around the tertiary star well.

While this phenomenological prescription was motivated by the Apep system, it can, in principle, be applied to other hierarchical triples hosting W-R CWBs. Unfortunately, W-R CWBs that can be resolved, i.e., directly imaged, are exceedingly rare with only a handful in the Galaxy. Hierarchical triple variants of these, especially those whose tertiary companion is close enough to sculpt surviving and bright dust, are rarer still. At present, there appear to be only two other confirmed hierarchical triple CWBs hosting W-R stars: WR 104 (D. J. Wallace et al. 2002; A. Soulain et al. 2018) and WR 147 (L. F. Rodríguez et al. 2020). For the former, the tertiary star seems too distant to affect the spiral dust plume, and radio imagery of the latter implies that the tertiary shock does not affect the spiral nebula. Still, this cavity prescription may be useful in later studies should similar nebular morphology be observed in other systems.

ORCID iDs

Ryan M. T. White https://orcid.org/0009-0006-7054-0880
Benjamin J. S. Pope https://orcid.org/0000-0003-2595-9114
Peter G. Tuthill https://orcid.org/0000-0001-7026-6291
Yinuo Han https://orcid.org/0000-0002-2106-0403
Shashank Dholakia https://orcid.org/0000-0001-9145-8444
Ryan M. Lau https://orcid.org/0000-0003-0778-0321
Joseph R. Callingham https://orcid.org/0000-0002-7167-1819
Noel D. Richardson https://orcid.org/0000-0002-2806-9339

References

Abbott, D. C. 1978, ApJ, 225, 893
Antognini, J. M. O. 2015, MNRAS, 452, 3610
Antognini, J. M. O., & Thompson, T. A. 2016, MNRAS, 456, 4219
Astropy Collaboration, Price-Whelan, A. M., Lim, P. L., et al. 2022, ApJ, 935, 167
Astropy Collaboration, Price-Whelan, A. M., Sipőcz, B. M., et al. 2018, AJ, 156, 123
Astropy Collaboration, Robitaille, T. P., Tollerud, E. J., et al. 2013, A&A, 558, A33
Bloot, S., Callingham, J. R., & Marcote, B. 2022, MNRAS, 509, 475

Bradbury, J., Frostig, R., Hawkins, P., et al. 2018, JAX: composable transformations of Python+NumPy programs, 0.3.13, GitHub, http://github.com/google/jax
Callingham, J. R., Crowther, P. A., Williams, P. M., et al. 2020, MNRAS, 495, 3323
Callingham, J. R., Tuthill, P. G., Pope, B. J. S., et al. 2019, NatAs, 3, 82
Cantó, J., Raga, A. C., & Wilkin, F. P. 1996, ApJ, 469, 729
Crowther, P. A., & Evans, C. J. 2009, A&A, 503, 985
del Palacio, S., García, F., De Becker, M., et al. 2023, A&A, 672, A109
Driessen, L. N., Pritchard, J., Murphy, T., et al. 2024, PASA, 41, e084
Eatson, J. W., Pittard, J. M., & Van Loo, S. 2022a, MNRAS, 517, 4705
Eatson, J. W., Pittard, J. M., & Van Loo, S. 2022b, MNRAS, 516, 6132
Gayley, K. G. 2009, ApJ, 703, 89
Gräfener, G., Vink, J. S., de Koter, A., & Langer, N. 2011, A&A, 535, A56
Han, Y., Tuthill, P. G., Lau, R. M., & Soulain, A. 2022, Natur, 610, 269
Han, Y., Tuthill, P. G., Lau, R. M., et al. 2020, MNRAS, 498, 5604
Han, Y., White, R. M. T., Callingham, J. R., et al. 2025, ApJ, 994, 122
Harris, C. R., Millman, K. J., van der Walt, S. J., et al. 2020, Natur, 585, 357
Hastings, B., Langer, N., & Puls, J. 2023, A&A, 672, A60
Hattori, S., Garcia, L., Murray, C., et al. 2024, exoplanet-dev/jaxoplanet: Astronomical Time Series Analysis with JAX, v0.1.0, Zenodo, doi:10.5281/zenodo.10736936
Hoang, T., & Tram, L. N. 2019, ApJ, 877, 36
Hoang, T., Tram, L. N., Lee, H., & Ahn, S.-H. 2019, NatAs, 3, 766
Huijser, D., Goodman, J., & Brewer, B. J. 2015, arXiv:1509.02230
Hunter, J. D. 2007, CSE, 9, 90
Kells, L. M., & Kern, W. F. 1940, Plane and Spherical Trigonometry (2nd ed.; New York: McGraw Hill Book Company)
Lamberts, A., Dubus, G., Lesur, G., & Fromang, S. 2012, A&A, 546, A60
Lau, R. M., Eldridge, J. J., Hankins, M. J., et al. 2020, ApJ, 898, 74
Lau, R. M., Hankins, M. J., Han, Y., et al. 2022, NatAs, 6, 1308
Lau, R. M., Wang, J., Hankins, M. J., et al. 2023, ApJ, 951, 89
Lemaster, M. N., Stone, J. M., & Gardiner, T. A. 2007, ApJ, 662, 582
Lieb, E. P., Lau, R. M., Hoffman, J. L., et al. 2025, ApJL, 979, L3
Maeder, A., Georgy, C., Meynet, G., & Ekström, S. 2012, A&A, 539, A110
Marcote, B., Callingham, J. R., De Becker, M., et al. 2021, MNRAS, 501, 2478
Markley, F. L. 1995, CeMDA, 63, 101
Moens, N., Poniatowski, L. G., Hennicker, L., et al. 2022, A&A, 665, A42
Moore, T., Smartt, S. J., Nicholl, M., et al. 2023, ApJL, 956, L31
Murray, C. D., & Dermott, S. F. 1999, Solar System Dynamics (Cambridge: Cambridge Univ. Press)
Murray, N., Ménard, B., & Thompson, T. A. 2011, ApJ, 735, 66
Naoz, S. 2016, ARA&A, 54, 441
Parkin, E. R., & Pittard, J. M. 2008, MNRAS, 388, 1047
Richardson, N. D., Henson, M., Lieb, E. P., et al. 2025, ApJ, 987, 160
Rodríguez, L. F., Arthur, J., Montes, G., Carrasco-González, C., & Toalá, J. A. 2020, ApJL, 900, L3
Schirmer, T., Ysard, N., Habart, E., et al. 2022, A&A, 666, A49
Soulain, A., Lamberts, A., Millour, F., Tuthill, P., & Lau, R. M. 2023, MNRAS, 518, 3211
Soulain, A., Millour, F., Lopez, B., et al. 2018, A&A, 618, A108
Thomas, J. D., Richardson, N. D., Eldridge, J. J., et al. 2021, MNRAS, 504, 5221
Toonen, S., Hamers, A., & Portegies Zwart, S. 2016, ComAC, 3, 6
Tuthill, P. G., Monnier, J. D., & Danchi, W. C. 1999, Natur, 398, 487
Tuthill, P. G., Monnier, J. D., Lawrance, N., et al. 2008, ApJ, 675, 698
Usov, V. V. 1991, MNRAS, 252, 49
van Marle, A. J., Langer, N., Yoon, S. C., & García-Segura, G. 2008, A&A, 478, 769
Virtanen, P., Gommers, R., Oliphant, T. E., et al. 2020, NatMe, 17, 261
Wallace, D. J., Moffat, A. F. J., & Shara, M. M. 2002, in ASP Conf. Se. 260, Interacting Winds from Massive Stars, ed. A. F. J. Moffat & N. St-Louis (San Francisco, CA: ASP), 407
White, R. M. T. 2025, xenomorph: the Fastest Way to Model the Colliding Winds of Massive Binary Stars, v1, Zenodo, doi:10.5281/zenodo.15875502
White, R. M. T., & Tuthill, P. 2025, in Encyclopedia of Astrophysics, ed. Ilya Mandel (1st ed.; Amsterdam: Elsevier), 584
Williams, P. M., Marchenko, S. V., Marston, A. P., et al. 2009a, MNRAS, 395, 1749
Williams, P. M., Rauw, G., & van der Hucht, K. A. 2009b, MNRAS, 395, 2221
Williams, P. M., van der Hucht, K. A., van Wyk, F., et al. 2012, MNRAS, 420, 2526
Zhekov, S. A., & Petrov, B. V. 2025, A&A, 693, A266